Computer Methods and Programs in Biomedicine 267 (2025) 108775

Contents lists available at ScienceDirect

Computer Methods and Programs in Biomedicine

journal homepage: www.sciencedirect.com/journal/computer-methods-and-programs-in-biomedicine

Assessing the impact of magnetic nanoparticle assemblies on magnetic hyperthermia performance: A predictive study

Max Schoenen, Thomas Schmitz-Rode, Ioana Slabu *

Institute of Applied Medical Engineering, Helmholtz Institute, Medical Faculty, RWTH Aachen University, Pauwelsstraße 20, Aachen 52074, Germany

ARTICLE INFO

Keywords:
Magnetic nanoparticles
Magnetic hyperthermia
Stochastic Langevin simulations
Magnetic relaxations
Agglomeration
Magnetic dipole-dipole interactions

ABSTRACT

Background and objective: Magnetic hyperthermia-based therapies depend on heating performances of magnetic nanoparticles (MNP). Beyond specific MNP properties, dipole-dipole interactions resulting from the formation of MNP assemblies have a pivotal influence on heating performance. There is, however, limited understanding of the range of attributable negative and positive effects.

Methods: Numerical simulations were used to unravel the effect of various spherical, elongated assemblies as well as MNP chains on heating performance. An advancing front assembly generating method was combined with a stochastic Langevin simulation. Experimental values of a hyperthermia application to destroy hollow organ tumours with heatable stent fibres were used to validate simulation results.

Results: Limited impact of assembly size on the heating performance was observed, whereas assembly geometry was crucial. Spherical assemblies lead to a decrease in specific loss power while elongated assemblies and chains yielded up to eightfold increase compared to randomly dispersed MNP. The heating performance of elongated assemblies and chains was dependent on their major-minor axes ratios, excitation field amplitude and assembly orientation relative to the field direction. The simulations unravelled that chains dominated the heating of stent fibres.

Conclusions: The simulation is a valuable and versatile tool for the optimization of heating output of all sorts of MNP, which undergo structural changes in interaction with artificial and biological surroundings. This capability is demonstrated for fibre-based implants with incorporated MNP. Comparison between simulation and experiments demonstrates the susceptibility to the design of MNP assemblies. Precise information about assembly geometry is crucial to improve the prediction accuracy.

1. Introduction

Due to their unique dynamic magnetic relaxation response to alternating magnetic fields, magnetic nanoparticles (MNP) enable local overheating of tissue, so-called magnetic hyperthermia (MH), which is a promising approach in cancer treatment [1–4]. Hyperthermia therapy approaches are based on injection of MNP at the target site, e.g. directly into a tumour, or on application of implantable devices, e.g. hybrid implants with incorporated MNP acting as heating agents inside the implants [1,2,5]. For example, hybrid stents were investigated for the treatment of hollow organ tumours and magnetic scaffolds were applied in bone cancer therapy [2,6]. Exposed to an alternating magnetic field (AMF), MNP generate heat, however, this exposure is so far not locally selective. MNP have already been established as contrast agents in magnetic resonance imaging (MRI) and are currently under development as tracers for magnetic particle imaging (MPI) [3,7–10]. Novel theranostic approaches envisage to combine MH with MPI [3,11–13]. Such a combination will allow selective image-guided therapies with a single device. Either way, MNP interact with their environment and this interaction has a tremendous impact on their performance as magnetic heating agents and tracers. Upon the internalization into cells and incorporation into implants, MNP tend to assemble into clusters [2,6,14,15]. In such cases, significant effects on their heating performance have been observed [16–20]. These are related to dipole-dipole interactions and the absence of Brownian relaxation. To account for these phenomena, the so-called Cole-Cole model, an extension of the Debye model used in linear response theory, was proposed [21,22]. With the Cole-Cole model it was possible to explain the temperature rise of magnetic scaffolds in an AMF as it considers a spectrum relaxation time resulting from interactions between MNP. For an accurate prediction of

* Corresponding author.
E-mail address: slabu@ame.rwth-aachen.de (I. Slabu).

https://doi.org/10.1016/j.cmpb.2025.108775
Received 18 December 2024; Received in revised form 29 March 2025; Accepted 10 April 2025
Available online 11 April 2025

MNP heating and tracer performance, interparticle and matrix interaction effects must be considered. Consequently, accurate predictions play a tremendous role as they ultimately influence the development of reliable and effective therapies.

Mainly a loss of heating performance upon environmental changes like cell internalization was identified to originate on the one hand from immobilization of MNP and on the other hand from magnetic interparticle interactions [20,23]. The interactions lead to a change of the magnetic relaxation response of MNP [24]. In many cases, higher energy barriers need to be overcome for magnetic relaxations processes to occur that lead to an effective heating. Depending on the properties of MNP, their assembly and applied magnetic field parameters an increase in heating output can be achieved [25,26]. For example, MNP chain structures have shown to enable significant increase of heating performance [27–29].

For the estimation of the heating output, simulation approaches have already shown to generate valuable information on MNP heating response and yield good accordance with experimental data [30–32]. They help to interpret experimental results and get a deeper insight into relevant mechanisms for heat generation. However, it is still an ongoing discussion, whether MNP assemblies and the resulting interparticle interactions lead to a decrease or increase of heating performance. It lacks a common understanding of the relation between different MNP assemblies and their heating performance.

In this work, we simulate the heating performance of different geometries of MNP assemblies. These simulations are a powerful tool for the prediction of the magnetic relaxation response of interacting MNP and deliver valuable information for the optimization of MNP as magnetic heating agents of hybrid implant design for targeted therapies. Further, a broader understanding on the influence of magnetic interparticle interactions on heating output is generated. Favourable combinations of magnetic field strengths and MNP assembly (chains, spherical assemblies, elongated assemblies) to get a high heating output are derived. The prediction models are based on stochastic non-equilibrium Langevin micro-magnetic simulations using the Landau-Lifshitz-Gilbert equation and include magnetic relaxation mechanisms as well as relaxations due to thermal fluctuations [10]. Compared to previous works, interparticle magnetic interactions between all simulated MNP are included. In this way, the effects on heating output based on magnetic dipole-dipole interaction between MNP can be clearly identified. Different geometries of MNP assemblies are generated according to a modified advancing front method [33]. This makes the simulation versatile in adjusting the MNP assembly geometry to resemble different material states and application conditions.

2. Methods

The simulations predict the influence of MNP assemblies on the heating performance. The measure for the heating output is the specific loss power (*SLP*) defined as the absorbed power per unit mass of MNP. Heating output results from magnetic relaxation processes of MNP exposed to alternating magnetic fields (AMF). The simulation is implemented in python and is based on the software described in previous works [10,32,34]. The availability of the software is described in the data statement. Currently the simulation without assembly formation (see Section 2, step 2) takes about 2–3 h. As depicted in Fig. S1 of the supplementary material the simulation can be divided into the following six steps:

1. Relevant parameters are set. These parameters can be divided into the four categories “MNP Parameters”, “Simulation Parameters”, “Field parameters”, and “External Parameters”. MNP parameters are the magnetic anisotropy constants K, core diameter d, hydrodynamic diameter d_H (by default set to 20 nm), saturation magnetization M_S (by default set to 420 kA/m), mass density of MNP ρ (by default set to 5180 g/cm^3) and concentration C (number of MNP in a defined space; arbitrarily large chosen to 10^{15} MNP/m^3 to avoid random agglomerations). The MNP parameters also include the log-normal distribution parameters for K, d and d_H (by default set to σ_K=0.05, σ_d=0.1 and σ_{dH}=0.2 to include distribution, corresponding to empirical values). The simulation parameters are the number of MNP M (by default set to 1000), time steps N_t (by default set to 10,000), magnetization cycles I (by default set to 2) and simulation repetitions X (by default set to 20; parallel execution on a HPC cluster). Field parameters are the field amplitude H_0 and frequency f. Finally, the external parameters are the temperature T (by default set to 300 K) and the viscosity η (by default water) of the surrounding material.
2. Simulation is initialized. To each MNP a core diameter, a hydrodynamic diameter and an anisotropy constant is attributed randomly drawn from a log-normal distribution. Further, to each MNP a magnetic moment $\boldsymbol{m}_i$ and easy axis $\boldsymbol{n}_i$ orientation is attributed drawn randomly from a normal distribution. Then the MNP are either randomly dispersed or assembled to different structures. Assemblies can be chains, spheres, or elongated assemblies with defined aspect ratios of the major and minor axes lengths. They are generated based on an advancing front algorithm [33]. It is intended to generate roughly densely packed MNP assemblies with a predefined size and geometry. In the assemblies the MNP have a predefined distance Δd to each other an. The advancing front algorithm consists of the following steps:
   a. One MNP of the predefined number M of lognormal distributed MNP is placed at a random position. A second MNP is placed at a predefined distance Δd and at a random spatial orientation relative to the first MNP. The positions of these two MNP form the initial list of MNP in the current assembly $\boldsymbol{F}$.
   b. A MNP p_F is chosen randomly from $\boldsymbol{F}$. A MNP p_V is chosen randomly from all MNP to be simulated. p_V is implemented at a distance Δd in a random relative orientation to p_F.
      i. p_V is added to $\boldsymbol{F}$ if the following conditions are fulfilled:
         - it does not overlap with another MNP in $\boldsymbol{F}$
         - it has a maximum distance of $\Delta d \pm \Delta$ with a tolerance margin $\Delta = 0.15$ nm to at least one other MNP in $\boldsymbol{F}$.
         - its position lies within the predefined dimensions of the desired assembly.
      ii. If p_V *does* not fulfil the conditions, it is discarded, and the program returns to step (b).
   c. An assembly generation is finished if for $N_{break} = 150$ times no MNP can be added to $\boldsymbol{F}$ or the number of MNP to be simulated is reached. In the former case, the generation of the next assembly is started. In the latter case, it is proceeded with step 3 of the simulation (see Fig. S1).
3. Before the “main simulation” (see step 4), a so-called thermalization is performed. It is equivalent to the main simulation but without an applied alternating magnetic field. For a defined number of timesteps $N_t/5$ the magnetic moments and anisotropy constants relax into a state solely defined by thermal activation and magnetic interactions between the MNP.
4. The main simulation is performed. At each time step, two stochastic Langevin differential equations (SDEs), Eqs. (1) and (2), are solved and the values of magnetic moments $\boldsymbol{m}_i$ and easy axes $\boldsymbol{n}_i$ of the MNP are updated and saved for each time step. The differential equations model the Néel relaxation (Landau-Lifshitz-Gilbert equation),

$$d\boldsymbol{m}_i/dt = \gamma_0/(1+\alpha^2)\cdot(\boldsymbol{H}_{eff}\times\boldsymbol{m}_i + \alpha\cdot\boldsymbol{m}_i\times(\boldsymbol{H}_{eff}\times\boldsymbol{m}_i)) \quad (1)$$

and the Brownian relaxation,

$$d\boldsymbol{n}_i/dt = \boldsymbol{\Theta}/(6\eta V_H) \times \boldsymbol{n}_i. \quad (2)$$

The effective field, $\boldsymbol{H}_{eff}$,

$$\boldsymbol{H}_{eff} = -1/\mu_0\cdot\partial U/\partial\boldsymbol{m} + \boldsymbol{H}_{th} \quad (3)$$

and the generalized torque, $\boldsymbol{\Theta}$,

$$\boldsymbol{\Theta} = (\partial U / \partial \boldsymbol{n}) \times \boldsymbol{n} + \boldsymbol{\Theta}_{\mathrm{th}} \tag{4}$$

are derived from the internal energy $U = \varepsilon_{\mathrm{Zee}} + \varepsilon_{\mathrm{Ani}} + \varepsilon_{\mathrm{IA}}$. This consists of the Zeeman energy $\varepsilon_{\mathrm{Zee}} = m \bullet H_{\mathrm{app}}$, the anisotropy energy $\varepsilon_{\mathrm{Ani}} = K \bullet V_{\mathrm{C}} \bullet (\boldsymbol{m}_{\mathrm{i}} \bullet \boldsymbol{n}_{\mathrm{i}})^2$ and the dipole-dipole-interaction energy, $\varepsilon_{\mathrm{IA}}$:

$$\boldsymbol{\varepsilon}_{\boldsymbol{IA}} = -\sum_{i} \boldsymbol{\mu}_0 \Big/ 4\pi \boldsymbol{r}_i^3 \cdot \left(3(\boldsymbol{m}_0 \cdot \boldsymbol{r}_i) \cdot (\boldsymbol{m}_i \cdot \boldsymbol{r}_i) / \boldsymbol{r}_i^2 - \boldsymbol{m}_0 \cdot \boldsymbol{m}_i\right). \tag{5}$$

The terms $\boldsymbol{H}_{\mathrm{th}}$ and $\boldsymbol{\Theta}_{\mathrm{th}}$ represent the gaussian-distributed thermal activation.

The SDEs Eqs. (1) and (2) are numerically integrated with the so-called Stratanovich–Heun method [10,35,36].

5. For each time step of the simulation, the z-component of the magnetic moment m_z is averaged over the ensemble of MNP.
6. After X iterations of the simulation, the magnetic moments are averaged over the iterations and plotted against magnetic field amplitudes for each time step resulting in a hysteresis curve. From the area A of the hysteresis curve, the *SLP* value is calculated as follows:

$$SLP = (A \cdot f) / \rho \tag{6}$$

3. Results

3.1. MNP assembly geometries

In the following, the results of the investigation of different MNP assembly geometries on the heating output are presented. Three MNP assemblies were generated (see Fig. 1): chains, spherical and elongated assemblies. For each assembly type, the influence of their size in relation to the field strength of the applied AMF was investigated and compared to that of randomly dispersed MNP.

The basic assumption is that the interparticle interactions in an assembly affects the reaction of MNP magnetic moments to the magnetic excitation field. Increasing the number of MNP in an assembly should correspondingly have a stronger impact on the *SLP* value since the interaction strength should increase. Whether the increase in L leads to an increase in the *SLP* value depends strongly on the applied excitation field amplitude (see Fig. 2a). At higher excitation field amplitudes, magnetic relaxations are more likely to occur. In this case, a strong increase in *SLP* value was observed, which is attributed to a collective relaxation of the magnetic moments of the interacting MNP. Reducing the field amplitude results in an initial SLP increase followed by a decrease to a saturation value. A further field amplitude reduction finally leads to a decrease in SLP below the value obtained for equivalent dispersed MNP and saturating at negligible values. The necessary field amplitude to obtain a strong magnetic relaxation response depends on the MNP size (see Fig. S2 in supplementary material), as the interparticle interaction strength varies with MNP size (see Eq. (5)). The length of the chain L was varied between one and 40 MNP per chain. As shown in Fig. 2a, increasing L up to ten MNP per chain changes the *SLP* values, while a further increase of L leads to saturation.

For the spherical assemblies, the diameter D_{C} was varied starting with an individual MNP and reaching an assembly size of 200 nm. Fig. 2b shows that *SLP* values of spherical MNP assemblies with a diameter D_{C} larger than four times the diameter of the individual MNP decreases below the value of randomly dispersed MNP. Below this size range, the assemblies show a magnetic response, which is similar to that of a chain. Above an assembly diameter four times the diameter of individual MNP, a saturation in the *SLP* values is observed. For assemblies smaller than four times the MNP diameter, higher *SLP* values than the ones of the corresponding randomly dispersed MNP occur.

For elongated assemblies, their size significantly affects the *SLP* value as shown in Fig. 2c. More specifically, the *SLP* increases with the assembly aspect ratio between the lengths of the major axes and the minor axes. Especially for higher aspect ratios and field amplitudes, the *SLP* values for the elongated MNP assemblies exceed the *SLP* values obtained for randomly dispersed MNP. Then, similar magnetic interaction effects as for chains arise leading to a collective relaxation behaviour of the MNP. Comparing the results under the same conditions at a field amplitude of 70 kA/m the highest *SLP* value is four times smaller than the one for chains, however, about three times higher than the one for spherical assemblies.

In Fig. 2d the dependency of the *SLP* value for elongated assemblies on the orientation of the major axes of the assemblies relative to the direction of the applied field is displayed. The angle θ between the orientation of the assembly relative to the direction of the magnetic field is varied between 0° and 90° The maximal *SLP* value is obtained when the major axis orientation is parallel to the field direction. The lowest *SLP* value is achieved when the major axis and the field directions are perpendicular to each other.

In Fig. 3, for selected assembly states, the MNP magnetic response dependency on magnetic field frequency is displayed. The chosen frequency range is typical for magnetic hyperthermia applications. Based on the findings of the previous simulations, three assembly states were selected, for which the greatest impact on magnetic response is

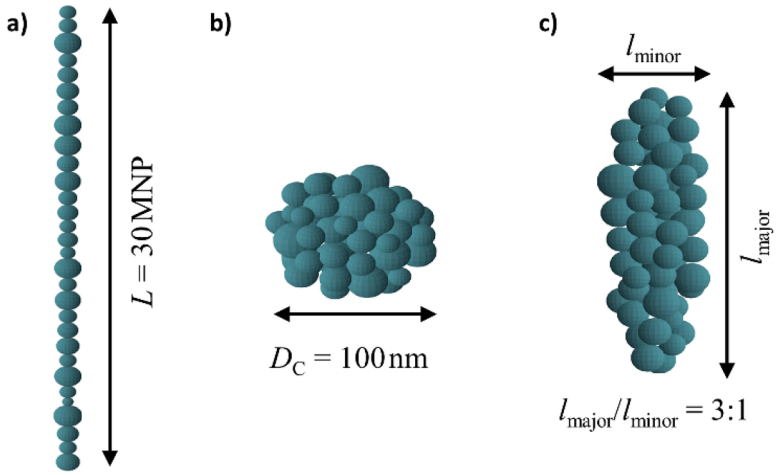

Fig. 1. Sketch of (a) an MNP chain with an exemplary length of $L = 30$ MNP, (b) a spherical MNP assembly with a diameter of $D_{\mathrm{C}} = 100$ nm and (c) an elongated MNP assembly with an aspect ratio $l_{\mathrm{major}}/l_{\mathrm{minor}}$ of three between the major axis and the minor axes.

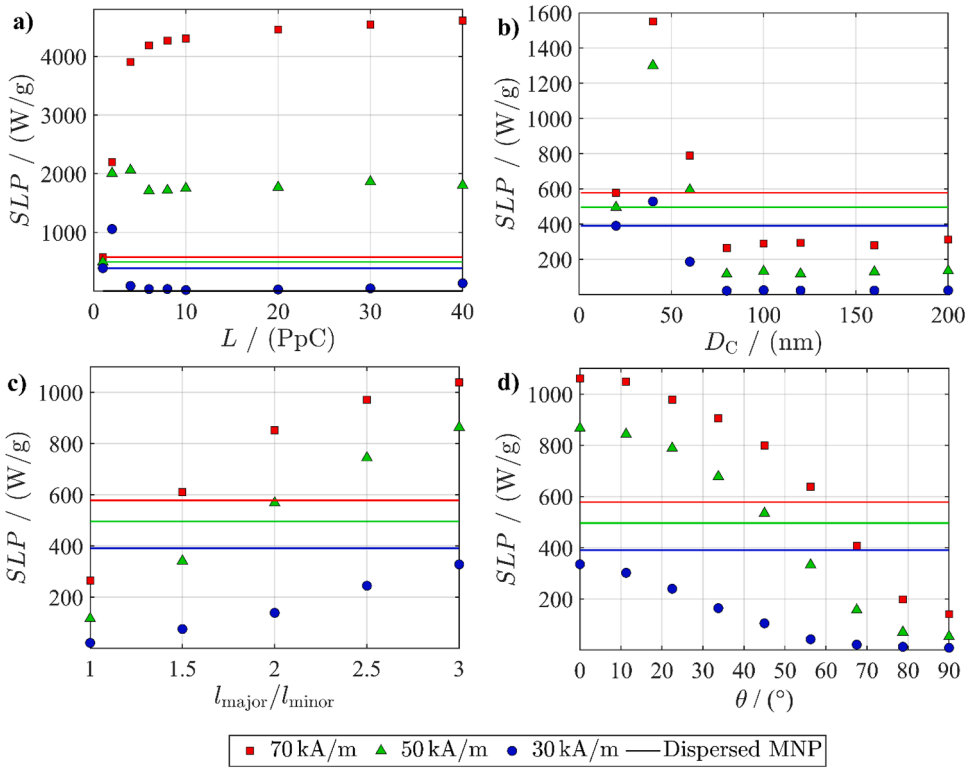

Fig. 2. (a) *SLP* versus the chain length *L*. Displayed are the results at three different magnetic field amplitudes. (b) *SLP* versus the assembly diameter D_C of spherical assemblies. (c) *SLP* versus the aspect ratio l_{major}/l_{minor} between the major and minor axis length of elongated MNP assemblies. (d) *SLP* versus the angle θ between the orientation of the elongated assemblies and the direction of the applied alternating magnetic field. The magnetic field frequency was set to $f = 300$ kHz. The simulations were performed for 20 nm MNP with an anisotropy constant of 11 kJ/m^3. For comparison, the *SLP* values from simulations of dispersed MNP ensembles are displayed as horizontal lines. The marker and line colour encode the applied field amplitude.

expected. This is estimated for assemblies with the largest length for chains, biggest diameter for spherical assemblies and highest aspect ratio for elongated assemblies. For better comparability, the $ILP = SLP/(f{\cdot}H^2)$ is calculated instead of *SLP* value. The ILP and the imaginary part of the susceptibility can be considered proportional to each other as the hysteresis area can be used for the calculation of both [37]. For all assembly types, the ILP value shows a local maximum, which is then followed by an increase towards saturation. In most cases, the local maxima are located at 50 kHz. Yet, for chains also a shift from 10 kHz (30 kA/m) to 50 kHz (50 kA/m) is visible. With increasing field amplitude, the local maxima disappear. For dispersed MNP, the highest *SLP* and *ILP* values are as expected at the highest frequency and field amplitude. For assemblies, the most favourable magnetic field settings to reach high *ILP* values strongly depends on the assembly state.

Fig. 4 summarizes the crucial impact of the MNP assembly geometry on the heating output for otherwise identical MNP properties and magnetic field parameters. The highest *SLP* values arise for chains, while the smallest arise for spherical assemblies. Especially at higher field amplitudes, elongated structures, and chains, which can be viewed as assembly structures with large aspect ratios, have favourable configuration to maximize the heating performance. In the case of chain structures, an up to eightfold *SLP* value compared to the one of dispersed MNP was reached at a high field strength of 70 kA/m. In contrast, at 30 kA/m a decrease of the *SLP* values by a factor of three compared to the one of dispersed MNP was found. This clearly demonstrates the strong influence of the interplay between assembly geometry and applied AMF on magnetic relaxation processes and consequently on heating performance.

3.2. Application example

To demonstrate the applicability of the simulation tool in predicting the heating output of MNP that change their structure after further processing into implants, simulations results were compared to experimental data, which was previously reported by the authors [2]. As discussed before, the experimental values of the heating output for the reference samples, i.e. dispersed MNP, are not useful anymore, as the MNP change their heating efficiency upon agglomeration and immobilization. Accordingly, the experimental data describes the heating efficiency of specific MNP agglomerations incorporated in fibre-based implants. As a result, for each implant and magnetic excitation configuration, new characterizations must be performed. An optimization of the implants for hyperthermia applications would be then costly and time consuming. The simulation provides insights into the dominating effects on heating output for the MNP incorporated in fibres and can predict heating output for different MNP configurations and magnetic field settings. In this way, the simulation gives valuable information on the optimization of the implants towards high heating efficiencies and supports the control of hyperthermia therapies for *in vivo* applications.

An exemplary picture of such agglomerated MNP inside fibres is shown in Fig. 5. Table 1 lists the AMF and MNP properties. In the simulation, MNP with saturation a magnetization and core diameters equivalent to those of the MNP in the experiment were used. In the experiments, different MNP weight percentages in the fibres (3 wt%, 5 wt% and 7 wt% MNP) were investigated showing differences in their heating output as shown in Fig. 6.

In the simulations, elongated MNP assemblies and MNP chains were investigated and compared. The aspect ratio was set according to the average aspect ratios reported before (see Table 1 and [2]). The simulated chain length value was derived from TEM images of the fibres (cf. exemplary TEM image in Fig. 5). For the simulations, the anisotropy constant was set to 20 kJ/m^3. This setting is based on preliminary considerations based on literature reports: The anisotropy constant of bulk magnetite is 11 kJ/m^3 [38]. For non-interacting spherical MNP

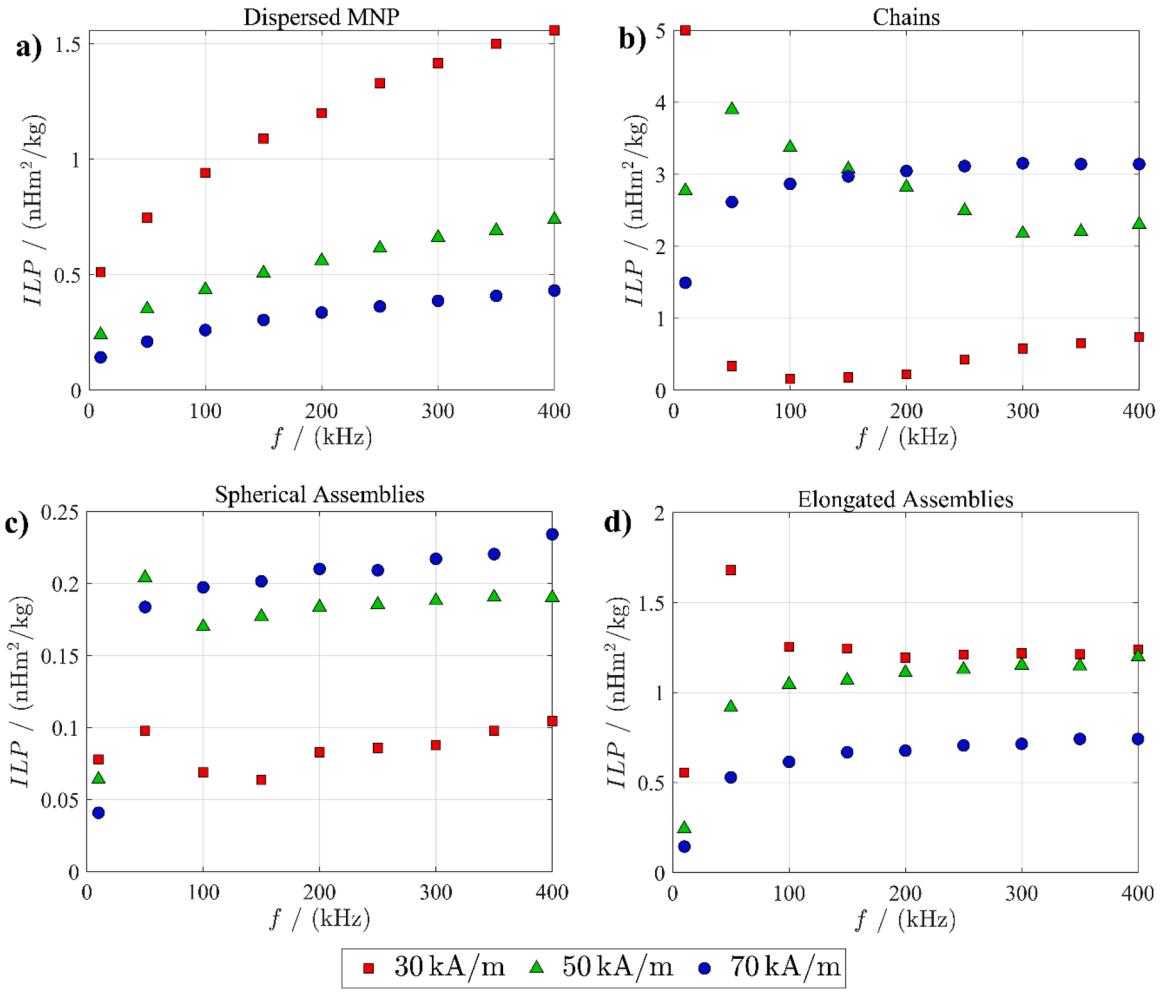

Fig. 3. *ILP* values vs. frequency at 30 kA/m, 50 kA/m and 70 kA/m for a) dispersed MNP, b) chains of 40 MNP, c) spherical assemblies with a diameter of 200 nm and d) elongated assemblies with a major axis length of 240 nm and a minor axis length of 80 nm. The MNP have a diameter of 20 nm and an anisotropy constant of 11 kJ/m^3.

with a core diameter of 17.7 nm, anisotropy constants between 10 kJ/m^3 and 20 kJ/m^3 were measured [39]. Magnetic interactions were shown to strongly influence the effective anisotropy. Along the same line, for non-interacting 10.2 nm MNP, comparable magnetic anisotropy values between 18.2 kJ/m^3 and 23.2 kJ/m^3 were determined via an extrapolation based of experimental values.

With magnetic interactions the values reached an effective anisotropy of up to ca. 100 kJ/m^3 [40]. The magnitude of the effective anisotropy was dependent on particle properties and distance between the MNP cores. In our simulation, an anisotropy constant of 20 kJ/m^3 was used. The contribution of interparticle interactions to effective anisotropy is regarded in the simulation by implementing dipole-dipole interactions. This value showed good agreement between predicted *SLP* values and experimental data.

Fig. 6 features the *SLP* values obtained from experiment compared to simulation data. The *SLP* values of elongated and chain-like MNP assemblies were investigated. The simulation results for an elongated assembly with a 2:1 aspect ratio and chains with a chain length of six MNP are shown. In the case of elongated assemblies, the simulation significantly underestimates the measured *SLP* values. Yet, the *SLP* values for the chain structures are in good agreement with the experimental data.

4. Discussion

In nearly all applications, agglomerations of MNP occur, e.g. in interaction with biological tissue or with an artificial matrix. These interactions cause deviations from the expected heating output, which in general is merely considered to be linear with MNP concentration and thus lead to a systematic error. Because of the outmost importance to control local heating in a therapeutical setting and to generate knowledge of what effects occur at nanoscale, we simulated the heating output for different agglomeration types integrating MNP interactions, i.e. in spherical and elongated agglomerations as well as chains. Beyond state of the art, our simulations uniquely combine directly calculated interparticle interactions, interconnected Brownian and Néel relaxations, random thermal contributions as well as the possibility to design different MNP structures of various shapes and sizes and to evaluate their heating output. The thermalization step (see Section 2, step 4) allows the MNP to relax into magnetic moment and easy axes states defined by the MNP assemblies rather than by a random initialization. Thus, it allows for example to account for gradual immobilization of MNP. This is especially interesting for agglomerations formation and disintegration in implants, scaffolds and cells, as it can be assumed that these are rather a continuous processes influencing the Brownian relaxation and thus the magnetic moment and easy axes states.

For chains, we observed a dependency of heating output, resembled in the *SLP* value, on the chain length *L,* which is strongly influenced by the field amplitude (see Fig. 2a). Due to the interparticle interactions, the magnetic moments of the MNP align parallel or antiparallel to the direction of the chain. The resulting dipolar magnetic coupling between

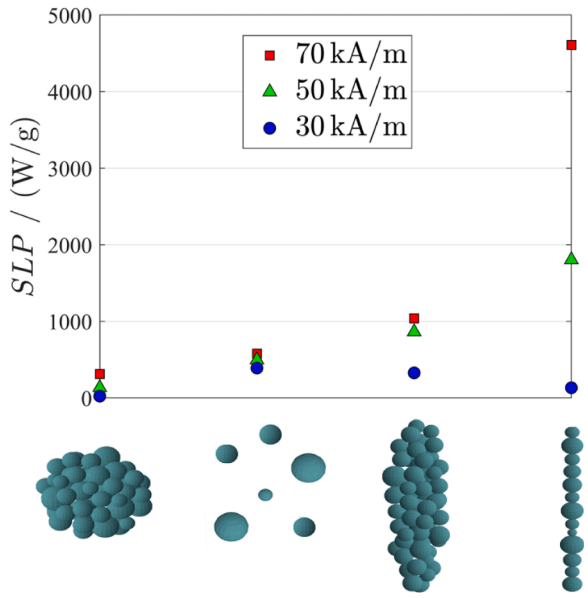

Fig. 4. *SLP* values obtained for spherical assemblies, randomly dispersed MNP, elongated assemblies and chains for different magnetic field amplitudes green (30 kA/m), orange (50 kA/m) and red (70 kA/m). The MNP have a diameter of 20 nm and an anisotropy constant of 11 kJ/m^3. The spherical assemblies have a diameter of 200 nm. The elongated assemblies have a major axes length of 240 nm and a minor axes length of 80 nm. The chains consist of 40 MNP. The magnetic field frequency is $f = 300$ kHz.

the MNP leads to an increase of the effective anisotropy (additional to contributions of magneto-crystalline, shape and surface anisotropy). This increase in the effective anisotropy in turn leads to a higher energy barrier, so that higher energy from the magnetic excitation field must be provided to induce magnetic moment relaxations. Consequently, the *SLP* is smaller at lower magnetic field amplitude of 30 kA/m.

Unlike chains, spherical assemblies show no preorientation of MNP magnetic moments. Correspondingly, no beneficial collective relaxation behaviour occurs to align their magnetic moments in the direction of the excitation field (see Fig. 2b). Rather magnetic frustrations of the MNP in the dense assembly lead to a demagnetizing effect. In general, the magnetic interparticle interactions between neighbouring MNP hinder the induction of magnetic relaxations by the applied alternating magnetic field. This is obvious when investigating the effects of distance between individual MNP in an assembly (i.e. choosing different packing densities) on heating output. Fig. S3 (supplementary material) shows that the influence of magnetic interactions gradually vanishes for larger interparticle distances and, hence, the *SLP* values of spherical assemblies converge towards the one of randomly dispersed MNP. These findings are consistent with experimental results reported in literature before [41]. A deviation from this trend occurs for agglomerations with a size smaller than four times the MNP diameter that lead to an SLP increase. In this case, the MNP assemblies are not radially symmetrically assembled, e.g. two MNP resemble a chain geometry. The overall trend of an initial increase of the *SLP* with an increase in agglomeration size followed by a steep decrease qualitatively fits to experimental findings for

Table 1
Properties of the MNP and of the alternating magnetic field used in the simulation: MNP core diameter d_{core}, saturation magnetization M_S, anisotropy constant of an individual MNP K, simulated MNP assembly configuration, frequency f of the magnetic field and the set field amplitudes H_0. The third column gives the source of information of the properties.

Property of simulated MNP	Values	Data source
$(d_{core} \pm \sigma_{core})$ / (nm)	11.3 ± 3.3	Experimental values [2]
M_S / (Am^2/kg(Fe))	99.4	Experimental values [2]
K / (kJ/m^3)	20	Typical value for non-interacting MNP [40]
Assembly configuration	Chains ($L = 6$ PpC) Elongated structures (l_{major} / l_{minor} = 2/1)	Typical values derived from TEM images [2]
f / (kHz)	270	Experimental setting [2]
H_0 / (kA/m)	10, 20, 30, 40, 55	Experimental settings [2]

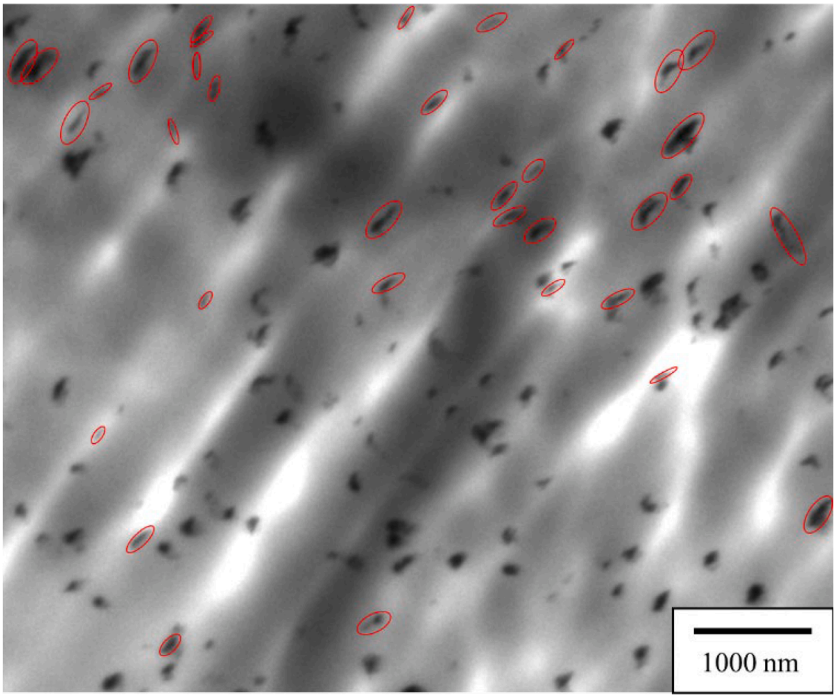

Fig. 5. Exemplary TEM image of a fibre with 3 wt% MNP. Agglomerations, which have a greater aspect ratio than 4:1 or show even chain-like structures are marked by red ellipses.

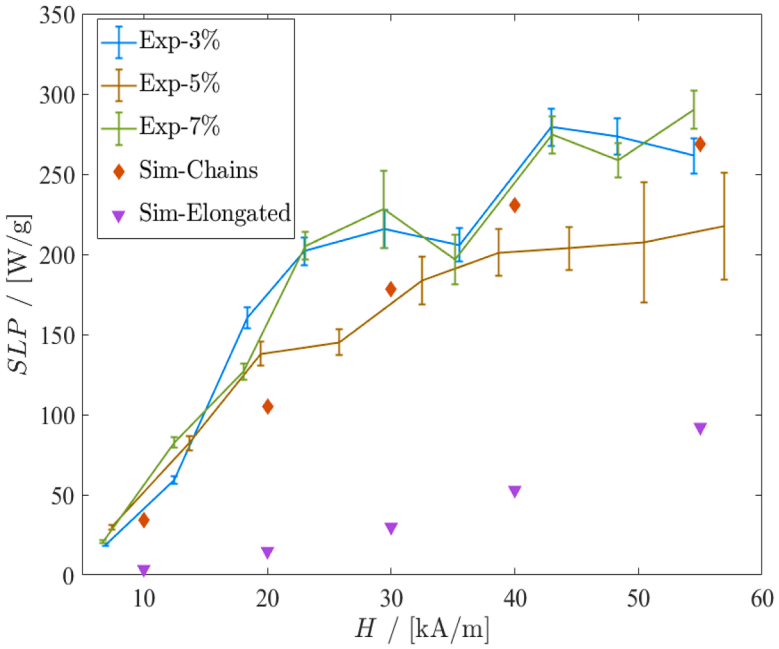

Fig. 6. *SLP* versus magnetic field amplitude. Displayed are experimental data and simulated data. The experimental data were acquired for immobilized MNP in fibres with three different MNP weight percentages (3 wt%, 5 wt% and 7 wt%). Simulated are two different types of MNP assembly structures: chains consisting of six MNP (Sim-Chains) and elongated assemblies with minor axes of 50 nm and a major axis of 100 nm (Sim-Elongated).

MNP agglomerations of increasing size [42]. Specifically, experimental data for MNP assembled in 3D centrosymmetric configurations showed smaller heating performance compared to their assembly in plane, i.e. 2D configuration [43,44].

For elongated assemblies, the increase in *SLP* with aspect ratio is linked to similar effects as the ones discussed for the chains (see Fig. 2c). Due to magnetic interactions and the assembly geometry, the magnetic moments align parallel or antiparallel to the major axis. Yet, compared to chains at small field amplitude of e. g. 30 kA/m no decrease in *SLP* occurs. This results from a less pronounced collaborative response of the MNP due to the not entirely straight alignment of the magnetic moments to the major axis compared to chain structures. Thus, SLP increase for increasing chain length is accelerated compared to the one for elongates assemblies. Further, the *SLP* of elongated assemblies decreases for increasing angle of the major axis relative to the direction of the applied magnetic field, θ (see Fig. 2d). Such an *SLP* dependency on the relative orientation of MNP assemblies to the magnetic field direction is also attained for chain structures (see Fig. S4 in supplementary material). When the major axis is rotated away from the magnetic field direction, the magnetic moments alignment in the direction of the major axes caused by interparticle interactions partially competes with the magnetic relaxation in the direction of the applied magnetic field.

The *ILP* dependence on frequency for the different MNP states (see Fig. 3) shows that the magnetic response strongly depends on assembly type. The results are in good agreement with literature reports [37]. The local maxima and their shift to higher frequencies for chains are only visible at low field amplitudes. This can be explained by a change in Néel relaxation time, which increases with field amplitude [22,37]. However, local maxima do not appear for all assembly types. This can be attributed to exponential increases in the Néel relaxation time with increasing effective anisotropies specific for each assembly type, which directly influences the non-linear dynamic magnetic susceptibility of the MNP [45].

The results of this work are in good agreement with experimental and simulation studies particularly concerning the effects of MNP chains on boosting heating output [27,46–48]. The dependency of the heating performance on chain length was observed for cubic MNP having different anisotropies specific to the edge lengths of individual MNP [46]. Further, it was shown that MNP form centrosymmetric spherical agglomerates inside cells leading to a reduction of heating efficiency [20]. To sum up, for otherwise identical MNP hyperthermia performance strongly depends on the assembly geometry, the excitation field amplitude as well as relative orientation of the assembly to the direction of the magnetic field. Our simulations provide an understanding of such effects and are a valuable tool to estimate the heating efficiency for all sorts of interacting MNP. Chains are preferable configurations to achieve high *SLP* values, however, they are difficult to realize in a therapeutical setting. The relative orientation of the MNP assembly major axis to the applied magnetic field direction may also be relevant for MPI. The dependence of the MPI signal on the MNP easy axes orientation has been shown in experiments [49].

The simulations performed to model experimental conditions for stent fibres with incorporated MNP agglomerations yield insights into the role of agglomeration structures for their heating performance. Surprisingly, chains describe the experimental data better than the elongated structures. This can be explained by the fact that a fraction of about 10 % of the assemblies have significantly higher aspect ratios (> 4:1) resembling chain-like structures (see Fig. 5). Similar strong impact of a small fraction of highly effective MNP on the overall heating performance of a whole MNP ensemble was reported before [47,50].

Consequently, the comparison between experimental and simulation data underlines the relevance of magnetic interparticle interactions for the achievable heating output in a magnetic hyperthermia application and explains the dominating effects on heating output. The experimental *SLP* values for the fibres with incorporated MNP at different concentrations (3 wt %, 5 wt % and 7 wt %) deviate especially at higher magnetic field amplitudes. This was not expected, since, by definition, the *SLP* value should not be dependent on MNP concentration (see Section 2). An explanation might be that for different MNP concentrations, specific differences in the MNP assembly geometry arise with a heterogeneity of MNP assemblies having different size and aspect ratios in the respective fibres. Generally, the magnetic coupling effects add to the effective magnetic anisotropy of the individual MNP. Depending on the experimental setting and sample preparation, the value of effective anisotropy constant varies. Consequently, in literature different anisotropy constants for assembly structures and for randomly dispersed MNP

were reported [47,51–53].

For more accurate predictions, precise information on structure and distribution of MNP assemblies inside the fibres is necessary. This can be acquired, e.g., by μCT-based measurements for bigger structures and by electron tomography for individual MNP in clusters [8,54,55]. Most valuable is, however, that the simulations provide information on what MNP configuration is best to enhance heating efficiency of nano-modified implants. This applies also to any other hybrid state of MNP and magnetic hybrid materials. For the investigated MNP in this work, the chain-like structures showed the best results. A control heat release from the implants can be realized by adjusting MNP configuration and the magnetic field parameters. The simulation does not include other types of interaction with the surrounding and is, therefore, not capable of estimating the heat dissipation.

Because of MNP immobilization in implants, Brownian relaxation is relevant only in thermalization step of the simulation. The effect of hydrodynamic diameter on the *SLP* value for MNP assemblies is then reduced to changing the interparticle distance (see Fig. S3). With increasing interparticle distance the *SLP* asymptotically approaches the *SLP* value for dispersed MNP, as dipole-dipole interactions are getting weaker. When considering MNP agglomeration in liquids, also a collective mechanical movement of the entire agglomerations plays an important role. To account for these phenomena, the simulation must be extended. This in turn increases the simulation time. Currently, the simulation time is already comparatively high (see Section 2). This limits the use of the simulation, e.g. in real-time applications such as image-guided interventions. As the calculations in the simulation involve large matrix operations, a GPU version might be beneficial for a simulation time reduction.

Beyond the application examples of hyperthermia in this work, the simulation software can be used to estimate the MNP performance in magnetic particle imaging [10]. Magnetic particle imaging combined with magnetic hyperthermia is envisaged as a promising hybrid modality for theranostic applications [3,56]. Consequently, the theranostic performance can be determined supporting treatment planning.

5. Conclusions

In this work, we employed a stochastic non-equilibrium simulation to unravel the influences of magnetic interparticle interactions within different MNP assemblies on their heating performance in a magnetic hyperthermia application. The results show that spherical assembly structures result in a decrease in heating output in comparison to the one obtained for randomly dispersed MNP. Strong magnetic interactions lead to an increase in the effective anisotropy and dynamic magnetic relaxation processes occur for chain structures at chain length specific higher field amplitudes. These effects are attributed to the parallel pre-orientation of magnetic moments to the major axis of the assembly resulting in a higher effective anisotropy, which competes with the energy needed to align the magnetic moments in the direction of the applied magnetic field. Similar effects were observed for elongated assembly structures at higher aspect ratios. For sufficient high magnetic field energies, chains and elongated assemblies yield a significant increase in heating output due to cooperative magnetic relaxation effects. Further, the highest heating output is achieved for MNP assemblies with the major axes aligned to the direction of the applied alternating magnetic field. The comparison with experimental data demonstrates that precise information on the MNP assembly configuration is crucial to accurately predict the heating performance. It was shown that even a small fraction of highly effective MNP strongly influences the overall heating performance. The results underline the impact of the geometry and the relative orientation of MNP assemblies to direction of the applied magnetic field on heating output. The simulations represent a valuable and versatile tool to estimate the heating performance for sorts of MNP configurations.

Glossary

AFM – alternating magnetic field
MH – magnetic hyperthermia
MNP – magnetic nanoparticles
MPI – magnetic particle imaging
SLP – Specific loss power
TEM – transmission electron microscopy

Data statement

The authors confirm that the data supporting the findings of this study are available within the article and its supplementary materials. The simulation is based on (https://github.com/cshasha/nano-simulate). The full code can be shared upon reasonable request.

Ethics statement

The research presented in this manuscript does not need an Ethics statement. No experimentation with animals or human subjects is contained.

CRediT authorship contribution statement

Max Schoenen: Writing – original draft, Visualization, Validation, Software, Conceptualization, Investigation, Formal analysis. **Thomas Schmitz-Rode:** Writing – review & editing, Resources. **Ioana Slabu:** Writing – review & editing, Visualization, Validation, Supervision, Resources, Project administration, Methodology, Funding acquisition, Conceptualization, Data curation.

Declaration of competing interest

The authors declare no conflict of interest. The funders had no role in the design of the study; in the collection, analyses, or interpretation of data; in the writing of the manuscript, or in the decision to publish the results.

Acknowledgements

We gratefully acknowledge financial support by the German Research Foundation (grant no. 467959793), by the Federal Ministry of Education and Research (grant no. 03VP10971) and by the European Union (ERC, MAD Control, 101076174). Views and opinions expressed are however those of the author(s) only and do not necessarily reflect those of the European Union or the European Research Council Executive Agency. Neither the European Union nor the granting authority can be held responsible for them. Simulations were performed with computing resources granted by RWTH Aachen University under project rwth0523 and project rwth1732. We thank Dmytrii Sachenko for the support in applying the simulation on the HPC cluster. We thank Eva Buhl form the Institute of Pathology, Electron Microscopy Facility, RWTH University Hospital Aachen for providing the TEM picture.

Supplementary materials

Supplementary material associated with this article can be found, in the online version, at doi:10.1016/j.cmpb.2025.108775.

References

[1] B. Mues, B. Bauer, J. Ortega, E.M. Buhl, H. Teller, T. Gries, T. Schmitz-Rode, I. Slabu, Assessing hyperthermia performance of hybrid textile filaments: the impact of different heating agents, J. Magn. Magn. Mater. 519 (2021) 167486, https://doi.org/10.1016/j.jmmm.2020.167486.
[2] B. Mues, B. Bauer, A.A. Roeth, J. Ortega, E.M. Buhl, P. Radon, F. Wiekhorst, T. Gries, T. Schmitz-Rode, I. Slabu, Nanomagnetic actuation of hybrid stents for

hyperthermia treatment of hollow organ tumors, Nanomaterials 11 (2021) 618, https://doi.org/10.3390/nano11030618.
[3] Z.W. Tay, P. Chandrasekharan, A. Chiu-Lam, D.W. Hensley, R. Dhavalikar, X. Y. Zhou, E.Y. Yu, P.W. Goodwill, B. Zheng, C. Rinaldi, S.M. Conolly, Magnetic particle imaging-guided heating using gradient fields for arbitrary localization of magnetic hyperthermia therapy, ACS Nano 12 (2018) 3699–3713, https://doi.org/10.1021/acsnano.8b00893.
[4] U.M. Engelmann, A.A. Roeth, D. Eberbeck, E.M. Buhl, U.P. Neumann, T. Schmitz-Rode, I. Slabu, Combining bulk temperature and nanoheating enables advanced magnetic fluid hyperthermia efficacy on pancreatic tumor cells, Sci. Rep. 8 (2018) 13210, https://doi.org/10.1038/s41598-018-31553-9.
[5] M.T. Basel, S. Balivada, H.W. Wang, T.B. Shrestha, G.M. Seo, M. Pyle, G. Abayaweera, R. Dani, O.B. Koper, M. Tamura, V. Chikan, S.H. Bossmann, D. L. Troyer, Cell-delivered magnetic nanoparticles caused hyperthermia-mediated increased survival in a murine pancreatic cancer model, Int. J. Nanomed. 7 (2012) 297–306, https://doi.org/10.2147/IJN.S28344.
[6] M.B. Lodi, N. Curreli, S. Zappia, L. Pilia, M.F. Casula, S. Fiorito, I. Catapano, F. Desogus, T. Pellegrino, I. Kriegel, L. Crocco, G. Mazzarella, A. Fanti, Influence of magnetic scaffold loading patterns on their hyperthermic potential against bone tumors, IEEE Trans. Biomed. Eng. 69 (2022) 2029–2040, https://doi.org/10.1109/Tbme.2021.3134208.
[7] L. Göpfert, M. Schoenen, O. Reisen, E.M. Buhl, B. Mues, T. Schmitz-Rode, I. Slabu, Enabling continuous flow manufacturing of magnetic nanoparticles with a millifluidic system, J. Magn. Magn. Mater. 563 (2022) 169985, https://doi.org/10.1016/j.jmmm.2022.169985.
[8] I. Slabu, N. Wirch, T. Caumanns, R. Theissmann, M. Krüger, T. Schmitz-Rode, T. E. Weirich, Electron tomography and nano-diffraction enabling the investigation of individual magnetic nanoparticles inside fibers of MR visible implants, J. Phys. D Appl. Phys. 50 (2017) 315303, https://doi.org/10.1088/1361-6463/aa77e8.
[9] B. Mues, E.M. Buhl, T. Schmitz-Rode, I. Slabu, Towards optimized MRI contrast agents for implant engineering: clustering and immobilization effects of magnetic nanoparticles, J. Magn. Magn. Mater. 471 (2019) 432–438, https://doi.org/10.1016/j.jmmm.2018.09.119.
[10] C. Shasha, K.M. Krishnan, Nonequilibrium dynamics of magnetic nanoparticles with applications in biomedicine, Adv. Mater. 33 (2021) 1904131, https://doi.org/10.1002/adma.201904131.
[11] P. Chandrasekharan, Z.W. Tay, D. Hensley, X.Y.Y. Zhou, B.K.L. Fung, C. Colson, Y. Lu, B.D. Fellows, Q. Huynh, C. Saayujya, E. Yu, R. Orendorff, B. Zheng, P. Goodwill, C. Rinaldi, S. Conolly, Using magnetic particle imaging systems to localize and guide magnetic hyperthermia treatment: tracers, hardware, and future medical applications, Theranostics 10 (2020) 2965–2981, https://doi.org/10.7150/thno.40858.
[12] D. Hensley, Z.W. Tay, R. Dhavalikar, P. Goodwill, B. Zheng, C. Rinaldi, S. Conolly, A theranostic platform for localized magnetic fluid hyperthermia and magnetic particle imaging, in: Proceedings of the Energy-Based Treatment of Tissue and Assessment IX 10066, 2017, pp. 10–17, https://doi.org/10.1117/12.2256350.
[13] T.A. Le, Y. Hadadian, J. Yoon, A prediction model for magnetic particle imaging-based magnetic hyperthermia applied to a brain tumor model, Comput. Methods Programs Biomed. 235 (2023) 107546, https://doi.org/10.1016/j.cmpb.2023.107546.
[14] N. Oh, J.H. Park, Endocytosis and exocytosis of nanoparticles in mammalian cells, Int. J. Nanomed. 9 (2014) 51–63, https://doi.org/10.2147/IJN.S26592.
[15] F. Spizzo, P. Sgarbossa, E. Sieni, A. Semenzato, F. Dughiero, M. Forzan, R. Bertani, L. Del Bianco, Synthesis of ferrofluids made of iron oxide nanoflowers: interplay between carrier fluid and magnetic properties, Nanomaterials 7 (2017) 373, https://doi.org/10.3390/nano7110373.
[16] U.M. Engelmann, E.M. Buhl, S. Draack, T. Viereck, F. Ludwig, T. Schmitz-Rode, I. Slabu, Magnetic relaxation of agglomerated and immobilized iron oxide nanoparticles for hyperthermia and imaging applications, IEEE Magn. Lett. 9 (2018) 1–5, https://doi.org/10.1109/LMAG.2018.2879034.
[17] G. Bëalle, R. Di Corato, J. Kolosnjaj-Tabi, V. Dupuis, O. Clément, F. Gazeau, C. Wilhelm, C. Ménager, Ultra magnetic liposomes for MR imaging, targeting, and hyperthermia, Langmuir 28 (2012) 11843–11851, https://doi.org/10.1021/la3024716.
[18] M. Jeun, S. Bae, A. Tomitaka, Y. Takemura, K.H. Park, S.H. Paek, K.W. Chung, Effects of particle dipole interaction on the ac magnetically induced heating characteristics of ferrite nanoparticles for hyperthermia, Appl. Phys. Lett. 95 (2009) 082501, https://doi.org/10.1063/1.3211120.
[19] N.A. Usov, Iron oxide nanoparticles for magnetic hyperthermia, Spin 9 (2019) 1940001, https://doi.org/10.1142/S2010324719400010.
[20] D. Cabrera, A. Coene, J. Leliaert, E.J. Artés-Ibáñez, L. Dupré, N.D. Telling, F. J. Teran, Dynamical magnetic response of iron oxide nano articles inside live cells, ACS Nano 12 (2018) 2741–2752, https://doi.org/10.1021/acsnano.7b08995.
[21] R. Hergt, R. Hiergeist, M. Zeisberger, G. Glöckl, W. Weitschies, P. Ramirez, I. Hilger, W.A. Kaiser, Enhancement of AC-losses of magnetic nanoparticles for heating applications, J. Magn. Magn. Mater. 280 (2004) 358–368, https://doi.org/10.1016/j.jmmm.2004.03.034.
[22] A. Fanti, M.B. Lodi, G. Mazzarella, Enhancement of cell migration rate toward a superparamagnetic scaffold using LF magnetic fields, IEEE Trans. Magn. 52 (2016), https://doi.org/10.1109/Tmag.2016.2583405. Artn 5200508.
[23] U.M. Engelmann, J. Seifert, B. Mues, S. Roitsch, C. Ménager, A.M. Schmidt, I. Slabu, Heating efficiency of magnetic nanoparticles decreases with gradual immobilization in hydrogels, J. Magn. Magn. Mater. 471 (2019) 486–494, https://doi.org/10.1016/j.jmmm.2018.09.113.
[24] D.P. Valdés, E. Lima, R.D. Zysler, G.F. Goya, E. De Biasi, Role of anisotropy, frequency, and interactions in magnetic hyperthermia applications: noninteracting nanoparticles and linear chain arrangements, Phys. Rev. Appl. 15 (2021) 044005, https://doi.org/10.1103/PhysRevApplied.15.044005.
[25] H. Khurshid, J. Alonso, Z. Nemati, M.H. Phan, P. Mukherjee, M.L. Fdez-Gubieda, J. M. Barandiarán, H. Srikanth, Anisotropy effects in magnetic hyperthermia: a comparison between spherical and cubic exchange-coupled FeO/Fe_3O_4 nanoparticles, J. Appl. Phys. 117 (2015) 17A337, https://doi.org/10.1063/1.4919250.
[26] R. Das, N.P. Kim, S.B. Attanayake, M.H. Phan, H. Srikanth, Role of magnetic anisotropy on the hyperthermia efficiency in spherical $Fe_{3-x}Co_xO_4$ (x=0-1) nanoparticles, Appl. Sci. 11 (2021) 930, https://doi.org/10.3390/app11030930.
[27] D. Serantes, K. Simeonidis, M. Angelakeris, O. Chubykalo-Fesenko, M. Marciello, M.D. Morales, D. Baldomir, C. Martinez-Boubeta, Multiplying magnetic hyperthermia response by nanoparticle assembling, J. Phys. Chem. C 118 (2014) 5927–5934, https://doi.org/10.1021/jp410717m.
[28] R. Fu, Y.Y. Yan, C. Roberts, Z.Y. Liu, Y.Y. Chen, The role of dipole interactions in hyperthermia heating colloidal clusters of densely-packed superparamagnetic nanoparticles, Sci. Rep. 8 (2018) 4704, https://doi.org/10.1038/s41598-018-23225-5.
[29] N.A. Usov, E.M. Gubanova, Application of magnetosomes in magnetic hyperthermia, Nanomaterials 10 (2020) 1320, https://doi.org/10.3390/nano10071320.
[30] D. Cabrera, A. Lak, T. Yoshida, M.E. Materia, D. Ortega, F. Ludwig, P. Guardia, A. Sathya, T. Pellegrino, F.J. Teran, Unraveling viscosity effects on the hysteresis losses of magnetic nanocubes, Nanoscale 9 (2017) 5094–5101, https://doi.org/10.1039/C7NR00810D.
[31] J.G. Ovejero, D. Cabrera, J. Carrey, T. Valdivielso, G. Salas, F.J. Teran, Effects of inter- and intra-aggregate magnetic dipolar interactions on the magnetic heating efficiency of iron oxide nanoparticles, Phys. Chem. Chem. Phys. 18 (2016) 10954–10963, https://doi.org/10.1039/C6CP00468G.
[32] U.M. Engelmann, C. Shasha, E. Teeman, I. Slabu, K.M. Krishnan, Predicting size-dependent heating efficiency of magnetic nanoparticles from experiment and stochastic Neel-Brown Langevin simulation, J. Magn. Magn. Mater. 471 (2019) 450–456, https://doi.org/10.1016/j.jmmm.2018.09.041.
[33] R.R. Valera, I.P. Morales, S. Vanmaercke, C.R. Morfa, L.A. Cortés, H.D.G. Casañas, Modified algorithm for generating high volume fraction sphere packings, Comput. Part. Mech. 2 (2015) 161–172, https://doi.org/10.1007/s40571-015-0045-8.
[34] U.M. Engelmann, C. Shasha, I. Slabu, Magnetic nanoparticle relaxation in biomedical application, Magn. Nanopart. Hum. Health Med. (2021) 327–354, https://doi.org/10.1002/9781119754725.ch15.
[35] S.A. Shah, D.B. Reeves, R.M. Ferguson, J.B. Weaver, K.M. Krishnan, Mixed brownian alignment and neel rotations in superparamagnetic iron oxide nanoparticle suspensions driven by an ac field, Phys. Rev. B 92 (2015) 094438, https://doi.org/10.1103/PhysRevB.92.094438. ARTN.
[36] J.L. García-Palacios, F.J. Lázaro, Langevin-dynamics study of the dynamical properties of small magnetic particles, Phys. Rev. B 58 (1998) 14937–14958, https://doi.org/10.1103/PhysRevB.58.14937.
[37] T. Yamaminami, S. Ota, S.B. Trisnanto, M. Ishikawa, T. Yamada, T. Yoshida, K. Enpuku, Y. Takemura, Power dissipation in magnetic nanoparticles evaluated using the AC susceptibility of their linear and nonlinear responses, J. Magn. Magn. Mater. 517 (2021), https://doi.org/10.1016/j.jmmm.2020.167401. ARTN 167401.
[38] L.R. Bickford, Ferromagnetic resonance absorption in magnetite single crystals, Phys. Rev. 78 (1950) 449–457, https://doi.org/10.1103/PhysRev.78.449.
[39] H. Mamiya, H. Fukumoto, J.L.C. Huaman, K. Suzuki, H. Miyamura, J. Balachandran, Estimation of magnetic anisotropy of individual magnetite nanoparticles for magnetic hyperthermia, ACS Nano 14 (2020) 8421–8432, https://doi.org/10.1021/acsnano.0c02521.
[40] P. García-Acevedo, M.A. González-Gómez, A. Arnosa-Prieto, L. de Castro-Alves, Y. Piñeiro, J. Rivas, Role of dipolar interactions on the determination of the effective magnetic anisotropy in iron oxide nanoparticles, Adv. Sci. 10 (2023) 2203397, https://doi.org/10.1002/advs.202203397.
[41] C. Guibert, V. Dupuis, V. Peyre, J. Fresnais, Hyperthermia of magnetic nanoparticles: experimental study of the role of aggregation, J. Phys. Chem. C 119 (2015) 28148–28154, https://doi.org/10.1021/acs.jpcc.5b07796.
[42] M. Jeong, S. Lee, D.Y. Song, S. Kang, T.H. Shin, J.S. Choi, Hyperthermia effect of nanoclusters governed by interparticle crystalline structures, ACS Omega 6 (2021) 31161–31167, https://doi.org/10.1021/acsomega.1c04632.
[43] S.K. Avugadda, M.E. Materia, R. Nismatullin, D. Cabrera, R. Marotta, T.F. Cabada, E. Marcello, S. Nitti, E.J. Artés-Ibañez, P. Basnett, C. Wilhelm, F.J. Teran, I. Roy, T. Pellegrino, Esterase-cleavable 2D assemblies of magnetic iron oxide nanocubes: exploiting enzymatic polymer disassembling to improve magnetic hyperthermia heat losses, Chem. Mater. 31 (2019) 5450–5463, https://doi.org/10.1021/acs.chemmater.9b00728.
[44] D. Niculaes, A. Lak, G.C. Anyfantis, S. Marras, O. Laslett, S.K. Avugadda, M. Cassani, D. Serantes, O. Hovorka, R. Chantrell, T. Pellegrino, Asymmetric assembling of iron oxide nanocubes for improving magnetic hyperthermia performance, ACS Nano 11 (2017) 12121–12133, https://doi.org/10.1021/acsnano.7b05182.
[45] G.T. Landi, F.R. Arantes, D.R. Cornejo, A.F. Bakuzis, I. Andreu, E. Natividad, AC susceptibility as a tool to probe the dipolar interaction in magnetic nanoparticles, J. Magn. Magn. Mater. 421 (2017) 138–151, https://doi.org/10.1016/j.jmmm.2016.08.011.
[46] H. Gavilán, K. Simeonidis, E. Myrovali, E. Mazarío, O. Chubykalo-Fesenko, R. Chantrell, L. Balcells, M. Angelakeris, M.P. Morales, D. Serantes, How size, shape and assembly of magnetic nanoparticles give rise to different hyperthermia

scenarios, Nanoscale 13 (2021) 15631–15646, https://doi.org/10.1039/D1NR03484G.
[47] B. Mehdaoui, R.P. Tan, A. Meffre, J. Carrey, S. Lachaize, B. Chaudret, M. Respaud, Increase of magnetic hyperthermia efficiency due to dipolar interactions in low-anisotropy magnetic nanoparticles: theoretical and experimental results, Phys. Rev. B 87 (2013) 174419, https://doi.org/10.1103/PhysRevB.87.174419.
[48] E. Myrovali, N. Maniotis, A. Makridis, A. Terzopoulou, V. Ntomprougkidis, K. Simeonidis, D. Sakellari, O. Kalogirou, T. Samaras, R. Salikhov, M. Spasova, M. Farle, U. Wiedwald, M. Angelakeris, Arrangement at the nanoscale: effect on magnetic particle hyperthermia, Sci. Rep. 6 (2016) 37934, https://doi.org/10.1038/srep37934.
[49] H. Albers, T. Knopp, M. Möddel, M. Boberg, T. Kluth, Modeling the magnetization dynamics for large ensembles of immobilized magnetic nanoparticles in multi-dimensional magnetic particle imaging, J. Magn. Magn. Mater. 543 (2022) 168534, https://doi.org/10.1016/j.jmmm.2021.168534.
[50] U.M. Engelmann, A. Shalaby, C. Shasha, K.M. Krishnan, H.J. Krause, Comparative modeling of frequency mixing measurements of magnetic nanoparticles using micromagnetic simulations and Langevin theory, Nanomaterials 11 (2021) 1257, https://doi.org/10.3390/nano11051257.
[51] S.L. Saville, B. Qi, J. Baker, R. Stone, R.E. Camley, K.L. Livesey, L.F. Ye, T. M. Crawford, O.T. Mefford, The formation of linear aggregates in magnetic hyperthermia: implications on specific absorption rate and magnetic anisotropy, J. Colloid Interface Sci. 424 (2014) 141–151, https://doi.org/10.1016/j.jcis.2014.03.007.
[52] F. Burrows, C. Parker, R.F.L. Evans, Y. Hancock, O. Hovorka, R.W. Chantrell, Energy losses in interacting fine-particle magnetic composites, J. Phys. D Appl. Phys. 43 (2010) 474010, https://doi.org/10.1088/0022-3727/43/47/474010.
[53] L.C. Branquinho, M.S. Carriao, A.S. Costa, N. Zufelato, M.H. Sousa, R. Miotto, R. Ivkov, A.F. Bakuzis, Effect of magnetic dipolar interactions on nanoparticle heating efficiency: implications for cancer hyperthermia, Sci. Rep. 3 (2013) 2887, https://doi.org/10.1038/srep02887.
[54] H. Rahn, S. Odenbach, X-ray microcomputed tomography as a tool for the investigation of the biodistribution of magnetic nanoparticles, Nanomedicine 4 (2009) 981–990, https://doi.org/10.2217/nnm.09.82.
[55] S. Odenbach, Microstructure and rheology of magnetic hybrid materials, Arch. Appl. Mech. 86 (2016) 269–279, https://doi.org/10.1007/s00419-015-1092-6.
[56] D. Hensley, Z.W. Tay, R. Dhavalikar, B. Zheng, P. Goodwill, C. Rinaldi, S. Conolly, Combining magnetic particle imaging and magnetic fluid hyperthermia in a theranostic platform, Phys. Med. Biol. 62 (2017) 3483–3500, https://doi.org/10.1088/1361-6560/aa5601.